



THE UNIVERSITY *of* EDINBURGH

Edinburgh Research Explorer

Multiscale numerical optimisation of hybrid metal/nonwoven shields for ballistic protection

Citation for published version:

Vila-Ortega, J, Ridruejo, A & Martinez-Hergueta, F 2019, 'Multiscale numerical optimisation of hybrid metal/nonwoven shields for ballistic protection', *International Journal of Impact Engineering*.
<https://doi.org/10.1016/j.ijimpeng.2019.103478>

Digital Object Identifier (DOI):

[10.1016/j.ijimpeng.2019.103478](https://doi.org/10.1016/j.ijimpeng.2019.103478)

Link:

[Link to publication record in Edinburgh Research Explorer](#)

Document Version:

Peer reviewed version

Published In:

International Journal of Impact Engineering

General rights

Copyright for the publications made accessible via the Edinburgh Research Explorer is retained by the author(s) and / or other copyright owners and it is a condition of accessing these publications that users recognise and abide by the legal requirements associated with these rights.

Take down policy

The University of Edinburgh has made every reasonable effort to ensure that Edinburgh Research Explorer content complies with UK legislation. If you believe that the public display of this file breaches copyright please contact openaccess@ed.ac.uk providing details, and we will remove access to the work immediately and investigate your claim.



Multiscale numerical optimisation of hybrid metal/nonwoven shields for ballistic protection

J. Vila-Ortega¹, A. Ridruejo¹, F. Martínez-Hergueta²

¹ *Department of Materials Science, Universidad Politécnica de Madrid, E. T. S. de Ingenieros de Caminos. 28040 - Madrid, Spain.*

² *School of Engineering, Institute for Infrastructure and Environment, University of Edinburgh, William Rankine Building, EH9 3FG, Edinburgh, UK.*

Abstract

This research presents a detailed numerical study of the ballistic performance of lightweight hybrid metal/nonwoven shields for automotive applications. Several configurations, including different number of nonwoven fabrics, were analysed to find the optimal design. Impact response of the nonwoven fabric was predicted by a multiscale numerical constitutive model able to capture its complex deformation and failure mechanisms: fibre straightening, realignment and disentanglement. Special attention was paid to the interaction between layers for different air gaps in the final energy absorption capacity of the shield, and detailed analysis of the different sequences of triggered failure modes was provided. The hybrid shield outperformed the previous configurations, resulting in an absorption capacity about twice the sum of the energies dissipated by the steel plates and the nonwovens individually. Furthermore, the hybrid shield increased the energy absorption capacity of the baseline steel plates by a factor over 8, with an almost negligible increment of areal weight of 5.5%, giving the possibility to improve the ballistic performance of conventional automotive components without penalising the fuel consumption of the vehicle.

Keywords: Ballistics, hybrid shields, nonwoven, finite element simulation

1. Introduction

During the last years, awareness of ballistic protection has been raised in the automotive industry. Although armoured vehicles have been extensively explored for defence [8, 19], the

27 high areal weight of conventional metal barriers penalises manoeuvrability and hinders their
28 implementation in the civilian automotive sector, where low fuel consumption and carbon
29 emissions are a priority. Areal weight can be drastically reduced by combining different
30 materials in a shield, taking advantage of the synergistic energy dissipation capability of
31 each component [21, 35, 34, 49]. As an example, the use of fibre-metal laminates is extended
32 from the aerospace sector to marine or civil engineering applications, where materials such
33 as GLARE are used for ballistic and blast protections [43, 38, 50, 14, 2]. For lower impact
34 energies, associated to smaller calibres and fragments, **dry fabrics with 100% content high**
35 **strength fibres offer a lightweight solution.** Polymeric fibres such as aramids (e.g. Kevlar)
36 and ultra-high molecular weight polyethylene (Dyneema) are now able to double the tensile
37 strength of high-strength steel, with one fifth of the areal weight of the metal plate [15, 1].
38 Depending on the disposition of the fibres in the material, they can be classified in woven
39 or nonwoven fabrics. In the former, fibres are bundled in weave yarns following a regular
40 pattern, while fibres form a disordered network in the latter [37]. Both materials are used
41 in ballistic protection [9, 33, 45, 7], however, the best performance against small fragments
42 is provided by nonwovens [4, 18, 47].

43 Hybrid metal/dry fabric shields are an innovative lightweight solution to arrest projec-
44 tiles. This system provides sufficient structural rigidity for components subjected to impact
45 loads and has been recently used for civil applications such as turbine engine fragment bar-
46 riers [42, 44]. Dry fabrics are usually placed in the front face of the target to redistribute
47 the load over the metal plate, changing the failure mode from plugging to petalling [15].
48 They are also placed in the rear face to absorb significant amount of energy by tensile de-
49 formation [5, 16]. Hybrid shields are usually combined with air gaps to improve the ballistic
50 performance [13, 46, 12]. Air gaps reduce the bending stiffness of the plates, changing their
51 failure mechanisms from shear to tensile modes, therefore, increasing the dissipated energy
52 compared to their bulk laminate counterparts. Considering the complexity of the interaction
53 between different plates and materials, numerical simulations are usually employed to pro-
54 vide a thorough insight of the coupled failure mechanisms [24, 25]. Finite element analysis
55 is a powerful tool which allows to explicitly combine all the target components and analyse

56 the failure sequence, with a higher accuracy than the one offered by high speed imaging.

57 It is possible to find multiple studies of metal/dry woven fabric shields in the litera-
58 ture, however, to the authors' knowledge, there are no applications for their counterpart
59 metal /nonwoven combination. In comparison, nonwoven fabrics present lower stiffness and
60 strength but higher deformability than their woven counterparts, resulting in an excellent
61 performance for small calibres and fragments. One of the reasons that hindered the inte-
62 gration of nonwoven materials into ballistic protections was the lack of understanding of
63 their micromechanical response, which resulted in low accuracy of the prediction of their
64 ballistic performance. Micromechanisms of deformation and fracture depend on the inter-
65 action of a number of factors including fibre uncurling, fibre reorientation as well as fibre
66 sliding and disentanglement, which are difficult to be captured by classical phenomenologi-
67 cal constitutive models [7]. Recent multiscale modelling efforts focused on the simulation of
68 needle-punched ultra-high molecular weight polyethylene nonwovens, providing a validated
69 simulation framework to accurately predict the ballistic response of the material in terms
70 of energy absorption and failure micromechanisms [30, 31]. These constitutive models were
71 recently employed to simulate the response of hybrid woven/nonwoven shields, showing the
72 potential of nonwovens to improve the ballistic performance of conventional barriers with
73 minimal increment in areal weight [32].

74 Considering the potential of nonwovens to improve the ballistic performance of conven-
75 tional components in the automotive sector, this investigation aims to provide a deeper
76 understanding on the ballistic performance of hybrid metal/nonwoven shields considering
77 several design parameters such as number of layers and air gaps. A virtual testing frame-
78 work by means of the Finite Element Method was developed to perform rigorous paramet-
79 rical studies. A conventional vehicle door composed by two thin steel plates was taken as
80 baseline configuration for this study. To this end, steel plates and nonwovens were mod-
81 elled, individually or in multilayer configurations, to characterise their ballistic response.
82 Special attention was paid to the interaction between layers in the final energy absorption
83 capacity of the target. The influence of the spacing was analysed for 2 and 3 nonwoven
84 layers targets on a wide range of distances, from 0.1 to 50 mm, showing the difference in ply

85 interaction, failure sequences and energy transfer mechanisms. The optimal configuration
86 was finally used to simulate the ballistic response of a hybrid metal/nonwoven vehicle door
87 composed by two external steel plates and three internal nonwovens. Ballistic performance
88 was analysed in terms of ballistic limit, energy absorption capacity and residual velocity
89 curves, showing the benefits of the hybrid configuration over the single material targets.

90 **2. Materials**

91 Two materials have been selected for the following study: an ultra-high molecular weight
92 polyethylene needle-punched nonwoven fabric and a commercial steel (ArcelorMittal 260BH)
93 for automotive industry. The resin free needle-punched nonwoven dry fabric is denominated
94 Fraglight NW201 (DSM) and it is manufactured by the continuous deposition of single
95 filaments of ultra high molecular weight polyethylene (Dyneema SK75) of approximately 60
96 mm in length on a moving bed surface forming a batt. The batt is needlefelted with the aid
97 of the oscillatory application of barbed needles, which introduce mechanical entanglements
98 among fibres [37]. The nominal areal density and thickness of the fabric, as given by the
99 manufacturer, are $\approx 190\text{-}220\text{ g/m}^2$ and $\approx 1.5\text{ mm}$, respectively.

100 The needlepunched process introduced two principal material orientations denominated
101 machine (MD) and transverse (TD) directions, which follow the bed displacement and its
102 orthogonal, respectively. The initial fibre orientation distribution function (ODF) was anal-
103 ysed in detail by means of 3D X-ray computed tomography (XCT) and 2D wide angle X-ray
104 diffraction (WAXD) and it was found to be isotropic [29]. Fibres were initially curved and
105 load was transferred within the fabric through the random and isotropic network of knots
106 created by needle-punching, leading to the formation of an active fibre network, see Fig.1(a).
107 Uncurling and stretching of the active fibres was followed by fibre sliding and pull-out from
108 the entanglement points. Most of the strength and energy dissipation was provided by the
109 extraction of the active fibres from the knots and final fracture occurred by the total disen-
110 tanglement of the fibre network in a given section at which the macroscopic deformation was
111 localized. Although the initial fibre ODF was isotropic, the in-plane mechanical properties
112 were highly anisotropic: the stiffness, strength and energy dissipated upon tensile deforma-

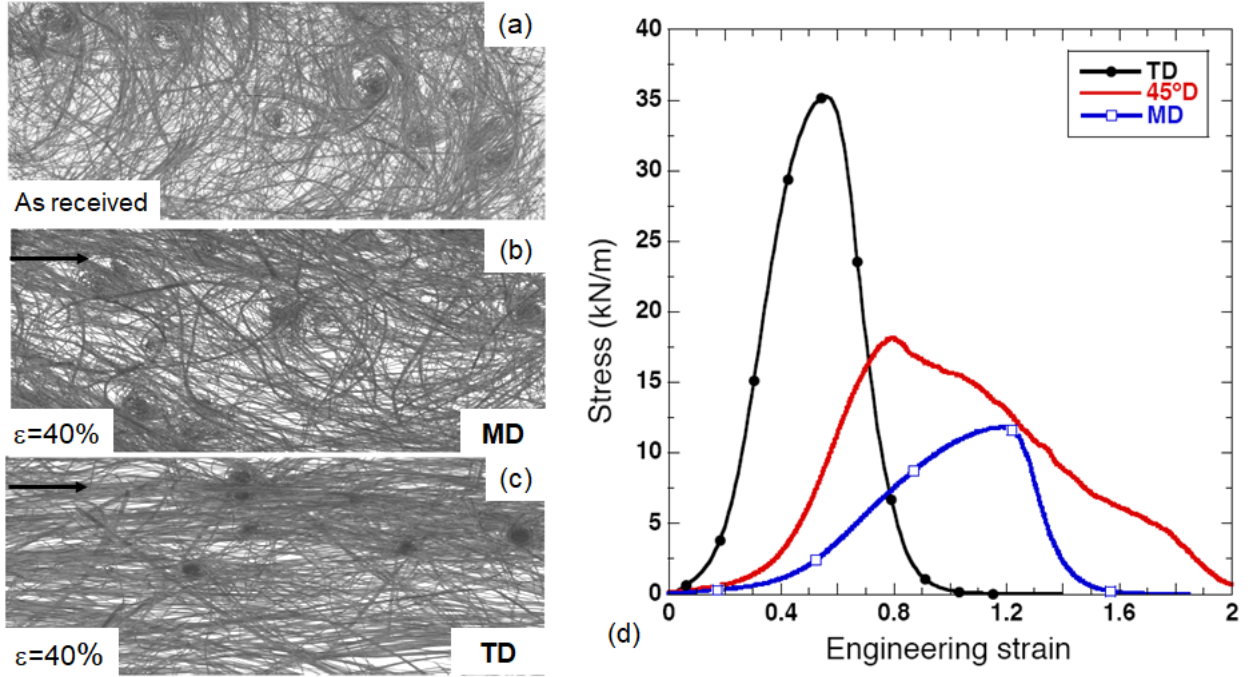


Figure 1: Evolution of the fibre ODFs of the nonwoven fabric with deformation. (a) As-received material, (b) after 40% of deformation along MD and (c) after 40% of deformation along TD. (d) Representative nominal stress (load per unit width) *vs.* engineering strain tensile curves in the fabric plane along the transverse direction (TD) and the machine direction (MD). Tests were carried out in square specimens of 100 x 100 mm² under quasi-static loading conditions [29].

113 tion in the TD were 2-3 times higher than those along MD, while the strain at maximum
 114 load along TD was only one half of that along MD, see Fig.1(d). This anisotropic behaviour
 115 was dictated by the microstructure evolution. Fibres tended to align towards the loading
 116 direction when the fabric was deformed along TD but minor fibre ODF evolution was ap-
 117 preciated during deformation along MD. Micromechanical pull-out tests indicated that the
 118 structure of the knots connected more fibres along TD than along MD and the better fibre
 119 interconnection led to a larger active fibre skeleton, enhancing the mechanical response along
 120 TD. In terms of affinity, fabrics deformed along TD essentially displayed affine deformation
 121 –i.e. most of the macroscopic strain was transferred to the fibres by the surrounding fabric–,
 122 while MD-deformed fabrics underwent non-affine deformation, and most of the macroscopic
 123 strain was not transferred to the fibres. Further information can be found in [29].

124 The ballistic performance of the nonwoven fabrics was characterized in detail in a pre-
125 vious publication [28]. The nonwoven dissipated the energy of the projectile by in-plane
126 deformation of the fabric leading to a cone of deformed material with an elliptical cross-
127 section due to the different wave propagation velocities along MD and TD, see Fig.2. The
128 deformation was accommodated by the same mechanisms observed during quasi-static in-
129 plane tensile deformation: load was transferred within the fabric through the random fibre
130 network, which included uncurling and rotation of the active fibres in the connected skeleton
131 followed by fibre sliding and pull-out from the entanglement points leading to a permanent
132 global deflection of the target until the projectile was arrested. In the tests carried out above
133 the ballistic limit, the final penetration of the target was accomplished by tearing as the
134 fibres were pulled out from the entanglement points and damage was localized around the
135 projectile.

136 The second material selected for this feasibility study was a commercial bake harden-
137 ing steel 260BH for automotive industry manufactured by Arcelor-Mittal [3]. Bake hard-
138 ening steels have been designed specifically for structural applications such as underbody
139 or reinforcement of lining. They promoted a significant increase in yield strength during
140 low-temperature heat treatments, particularly paint curing at 170 °C approximately, which
141 resulted in substantial weight reduction in all finished parts in the case of low forming
142 strains. They also possessed high deformability and improved dent resistance, which made
143 them suitable for impact applications. 0.7 mm thickness plates were chosen for the proposed
144 study, representative of the real thickness of a car door with a density of 7850 kg/m³ and
145 an equivalent areal weight of 5500 g/m².

146 **3. Computational modelling of impact on hybrid shields**

147 Numerical simulations of the ballistic impact on the steel plates, the nonwoven fabrics
148 and the multi-layered hybrid shield were performed to get a better understanding of the
149 deformation and fracture mechanisms during impact and optimise the ballistic performance.
150 Simulations were carried out using the finite element method in Abaqus/Explicit within the
151 framework of large displacements and rotations with the initial unstressed state taken as

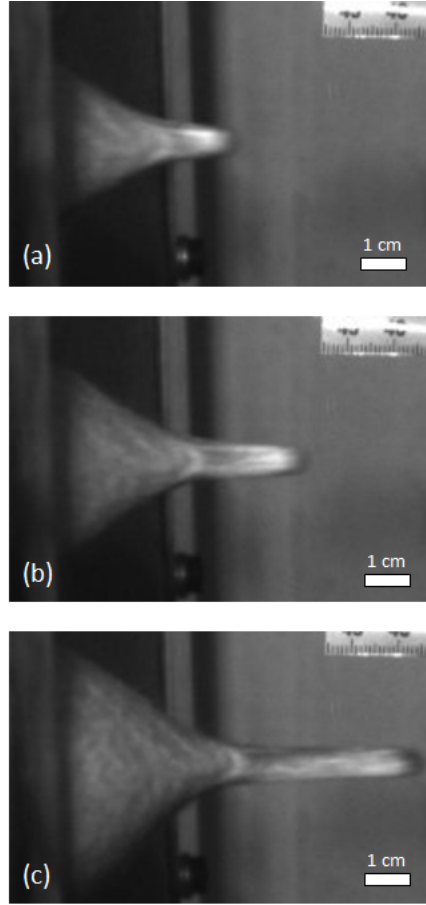


Figure 2: Deformation of the polyethylene nonwoven fabric during impact at 322 m/s, above the ballistic limit. (a) $t = 150 \mu\text{s}$, (b) $t = 225 \mu\text{s}$ and (c) $t = 350 \mu\text{s}$. Failure mode of the material was fibre disentanglement. [28]

152 reference. Different constitutive material models were used to describe the steel plates and
 153 the nonwoven fabrics as detailed below.

154 3.1. Constitutive model of steel plates

155 Bake hardening steel, after treatment, possess little strain rate sensitivity [10], so a
 156 standard isotropic linear hardening model (with Von Mises yield surface), available in the
 157 Abaqus/Explicit material library [11] was employed:

$$\sigma_y = \sigma_y^0 + H\varepsilon^{pl} \quad (1)$$

158 where σ_y defined the yield stress, σ_y^0 , its initial value, ε^{pl} the plastic deformation and H the
 159 hardening modulus. The elastic Young's Modulus, E , and the Poisson's ratio, ν , were also
 160 defined to compute the recoverable strains.

161 Failure of the material was established by the ductile failure criterion proposed in [17, 20],
 162 a phenomenological model for predicting the onset of damage due to nucleation, growth and
 163 coalescence of voids. The model assumed that the equivalent plastic strain at the onset of
 164 damage, $\bar{\varepsilon}_D^{pl}$, was a function of strain rate $\dot{\varepsilon}^{pl}$ and stress triaxiality ξ . In the particular case
 165 of the 260BH steel, a rate independent curve was defined with the tabular set of parameters
 166 included in Table 1.

167 The criterion for damage initiation was met when the following condition was satisfied:

$$\int \frac{d\bar{\varepsilon}^{pl}}{\bar{\varepsilon}_D^{pl}} = 1 \quad (2)$$

168 After the onset of damage, degradation of the material occurred. Numerically, it was
 169 implemented as a softening of the undamaged stress tensor, $\bar{\sigma}$, such as:

$$\sigma = (1 - d)\bar{\sigma} \quad (3)$$

170 The damage variable, d , ensured that the total energy dissipated after the onset of
 171 damage was equal to the fracture toughness of the alloy, Γ . To avoid any mesh dependency,
 172 the dissipated energy was normalised by the characteristic length of the finite element, L_{ch} :

$$\Gamma = \int_{\bar{\varepsilon}_0^{pl}}^{\bar{\varepsilon}_f^{pl}} L_{ch} \sigma_y d\varepsilon^{pl} = \int_0^{\bar{u}_f^{pl}} \sigma_y d\bar{u}^{pl} \quad (4)$$

173 where \bar{u}^{pl} stands for the equivalent plastic displacement, the fracture work conjugate of the
 174 yield stress after the onset of damage. The definition of the damage variable considering
 175 exponential softening was given as:

$$d = 1 - \exp\left(-\int_0^{\bar{u}_f^{pl}} \frac{\bar{\sigma}_y \dot{\bar{u}}^{pl}}{\Gamma}\right) \quad (5)$$

176 where $\dot{\bar{u}}^{pl}$ stands for the evolution of plastic displacement, and $\bar{\sigma}_y$ for the trial yield strength.
 177 Further information about the material model is available in [11] and material properties
 178 are summarized in Table 1. More details of the implementation are available in [48].

Table 1: Material parameters for Steel 260BH [48].

Density, ρ	7850 kg/m ³
Young's Modulus, E	200 GPa
Poisson's ratio, ν	0.27
Hardening Modulus, H	2.5 GPa
Ultimate Strength, σ_0	400 MPa
Yield Strength, σ_y	280 MPa
Strain to failure, ε_D^{pl}	0.3
Strain rate, $\dot{\varepsilon}^{pl}$	10 ⁶
Triaxiality, ξ	0.8
Fracture toughness Γ	0.072 J/mm ²

179 3.2. Constitutive model of nonwoven fabrics

180 The mechanical behaviour of the nonwoven fabric was given by a multiscale constitutive
 181 model previously developed, which was able to take into account the complex deformation
 182 and fracture mechanisms of this material under in-plane deformation and impact [30, 31].
 183 The model provided the mechanical response of a mesodomain of the nonwoven fabric, which
 184 corresponded to a finite element in the numerical simulation, and it is briefly recalled here
 185 for the sake of completion.

186 The model was divided in two blocks which dealt with the network and the fibre response.
 187 The network model established the relationship between the macroscopic deformation gra-
 188 dient \mathbf{F} and the microscopic response obtained by integrating the response of the fibres in
 189 the mesodomain that was formed by a planar square region of arbitrary size containing a
 190 random network of long, curly, non-interacting fibres, see Fig.3. The mechanical response
 191 of the mesodomain in terms of the second Piola-Kirchoff nominal stress tensor, \mathbf{S} , (force per
 192 unit width) was given by

$$\mathbf{S} = \int_{-\frac{\pi}{2}}^{\frac{\pi}{2}} \Psi(\beta_0) \sigma_f(\lambda) f_f(\beta_0) \frac{(\hat{\mathbf{n}} \otimes \hat{\mathbf{n}})}{\sqrt{\mathbf{C}\hat{\mathbf{n}} \cdot \hat{\mathbf{n}}}} d\beta_0 \quad (6)$$

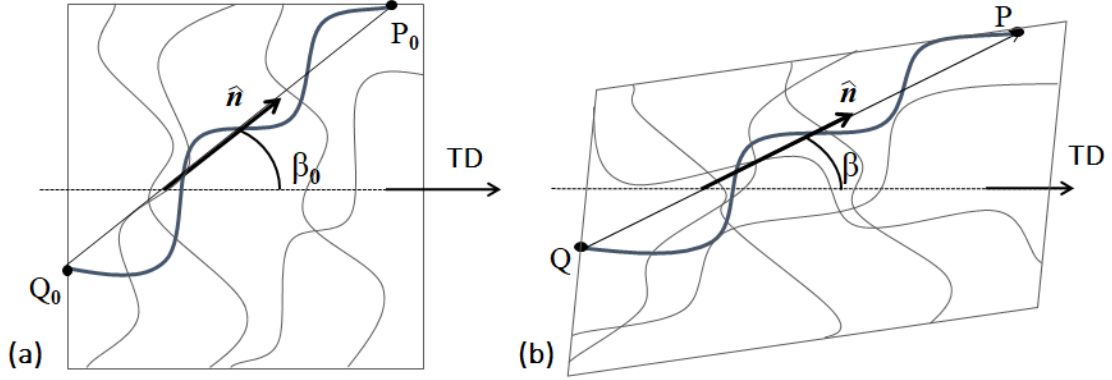


Figure 3: Schematic of the network mesodomain formed by different sets of curly fibres. (a) References and (b) deformed configurations [30].

193 where $\Psi(\beta_0)$ was the fibre orientation distribution function (ODF) in the reference con-
 194 figuration, $\sigma_f(\lambda)$ the stress carried by the fibre as a function of the stretch λ , $f_f(\beta_0)$ the
 195 active fibre length engaged in the deformation process, $\mathbf{C} = \mathbf{F}^T \mathbf{F}$ the right Cauchy-Green
 196 strain tensor, and $\hat{\mathbf{n}}$ a unit vector which formed an angle β_0 with respect to an arbitrary,
 197 privileged direction (e.g. the transverse direction TD of the nonwoven fabric) in the initial
 198 configuration.

199 The fibre model took into account the deformation features experimentally found for each
 200 set of fibres, including fibre uncurling and re-orientation, non-affine deformation, pull-out
 201 and disentanglement [29]. These mechanisms were introduced in a phenomenological model
 202 which characterised the stress (σ_f) - stretch (λ) behaviour of the fibre according to:

$$\begin{aligned} \sigma_f &= K [\eta(\beta_0)(\lambda - 1)]^3 & \sigma_{tr} < \sigma_{po} \\ \sigma_f &= (1 - d)K [\eta(\beta_0)(\lambda - 1)]^3 & \sigma_{tr} > \sigma_{po} \end{aligned} \quad (7)$$

203 where K was the fibre stiffness, $\eta(\beta_0)$ was the affinity parameter, which measured the per-
 204 centage of macroscopic deformation transmitted into the microstructure along each direction,
 205 σ_{po} the pull-out strength, d the damage parameter that accounted for the progressive reduc-
 206 tion in the load carried by the fibre during extraction from the fabric and σ_{tr} was a trial
 207 stress computed from the fibre stretch assuming no damage.

208 Once the fibre stress had attained the pull-out strength, σ_{po} , the pull-out process begun

209 and the load carried by the fibre decreased progressively until it was completely disengaged
 210 from the fabric. The stress carried by the fibres during this stage was determined by means
 211 of a continuum damage model, and it was function of the damage parameter d and of the
 212 fracture energy per unit fibre cross-section dissipated during pull-out, G . This fracture
 213 energy was obtained from the belt friction theory, and it was given by [30],

$$G = \frac{\sigma_{po} L_c}{\mu \theta} (1 - e^{-\mu \theta m_{po}}) \quad (8)$$

214 where L_c was the fibre length between entanglements, μ the friction coefficient, θ the fibre
 215 curvature and m_{po} the number of mechanical entanglements involved in the pull-out process.

216 In each time increment of the numerical simulation, the right stretch tensor \mathbf{U} was used
 217 to compute the stretch λ of each set of fibres. Each mesodomain of the fibre network (that
 218 coincides with a finite element with one Gauss point) was described by 65 sets of fibres
 219 with different orientation in the range $(-\frac{\pi}{2}, \frac{\pi}{2})$ and the second Piola-Kirchhoff nominal stress
 220 tensor, \mathbf{S} , was obtained by integrating eq.(6) along the different orientations. The fibre
 221 stretch λ for each fibre set was used to compute the trial stress σ_{tr} in the absence of damage,
 222 which was compared with the corresponding pull-out strength σ_{po} . The pull-out strength
 223 for each fibre set was chosen at the beginning of the simulation using a Monte Carlo lottery
 224 inside a given interval. If $\sigma_{tr} \leq \sigma_{po}$, $\sigma_{tr} = \sigma_f$ according to equation (7). If $\sigma_{tr} > \sigma_{po}$,
 225 the actual fibre stress σ_f was obtained from a continuum damage model depending on the
 226 damage variable d and the fracture energy, G , following eq. (7). A damage variable D was
 227 defined for each finite element (Gauss point) as the average damage of all fibre sets in the
 228 elements. The details of the numerical implementation of the damage model as well as of
 229 the crack band approach to obtain results that are independent of the finite element size can
 230 be found in [30]. The constitutive model parameters can be found in Table 2 and coincide
 231 with those used in previous investigations to predict the impact behaviour of the nonwoven
 232 fabric [27, 31, 32].

Table 2: Model parameters [30].

Fibre density, ρ_f	970 kg/m ³
Fibre length, L_{fiber}	60 mm
Bundle cross section, Ω	$1.27 \cdot 10^{-4}$ mm ²
Areal density, ρ	0.2 kg/m ²
Friction coefficient [40], μ	0.1
Initial fibre ODF, $\Phi(\beta_0)$	$1/\pi$
Initial fibre curvature, θ_0	π rad
Affinity, $\eta(\beta_0)$	Interpolation [1, 1/2] [30]
Active fibre length, $f_f(\beta_0)$	$0.223\eta(\beta_0)-0.084$ mm
Fibre stiffness, K	9.0 GPa
Pull-out strength, σ_{po}	[0.3, 1.7] GPa
Contour length, L_c	2.0 mm
Fibre pull-out length, L_{po}	60 mm
Critical value of the hydrostatic strain, (\hat{U}_{unl})	0.85

233 3.3. Numerical implementation and virtual impact testing

234 Steel plates and nonwoven layers were simulated individually and combined in hybrid
235 configurations to virtually optimise the ballistic performance of the hybrid metal/nonwoven
236 shield. Targets had a square shape of 350 x 350 mm² and all the lateral boundaries were
237 fully constrained during the impact simulation. The mesh was finer around the impact zone
238 (finite elements of 1 mm²) and the element size increased progressively with the distance
239 towards the clamped edges to reduce the computational cost. Steel plates were discretised
240 with S4R shell elements, reduced integration, hourglass control and finite membrane strain,
241 meanwhile nonwoven fabric layers were simulated by M3D4R membrane elements, reduced
242 integration, enhanced hourglass control and second order accuracy. Default Abaqus bulk
243 viscosity was used to minimise numerical instabilities. **The used of membrane elements to**
244 **simulate the mechanical response of dry woven fabrics has been previously validated [23, 41]**

245 and it is also a conventional approach to study nonwoven materials [6, 26, 31, 36]. The
246 impactor was modelled as a rigid sphere of 5.5 mm in diameter, density 7.85 g/cm³ and
247 0.706 g of mass. Contact between the different layers and the impactor was defined by
248 a softened tangential behaviour with an sticking friction slope of $\kappa= 0.001$ and a friction
249 coefficient $\mu=0.1$. Fully damaged elements ($D > 0.99$), were removed from the simulations
250 to avoid excessive element distortion. In the particular case of the metal plates, the damage
251 model available in Abaqus deleted the elements once the damage parameter achieved a value
252 equal to 0.99 [11]. In the case of the VUMAT subroutine for the nonwoven, elements were
253 deleted when the average damage variable (computed from the 65 individual fibre sets at
254 each Gauss point) achieved a value equal to 0.99.

255 The developed virtual testing framework was employed to accomplish a rigorous optimi-
256 sation exercise of the hybrid shields, focusing on the influence of the relative distance of the
257 nonwoven fabrics on the ballistic performance. Numerical simulations and tested configu-
258 rations are summarised in Table 3. First of all, the impact response of the steel plate and
259 the nonwoven fabric were analysed separately to determine their deformation and failure
260 mechanisms. Predictions of the ballistic performance of the nonwoven fabric were correlated
261 against previous experimental results [28]. Afterwards, parametrical studies on the relative
262 spacing between nonwoven layers were accomplished to determine the influence on the final
263 energy absorption capacity of the targets. Dependency of the energy dissipation with the
264 spacing between layers was characterised for a target consisting of two nonwoven layers with
265 variable spacing in the interval 0.1 to 50 mm every 2 mm at a fix impact velocity of 450
266 m/s, above the ballistic limit. Furthermore, ballistic limit and residual velocity curves for
267 selected spacings of 0.1, 10 and 50 mm were obtained for comparison purposes. This study
268 was additionally extended for three-layer systems with 10 mm spacing. Finally, a hybrid
269 shield consisting of 2 external steel plates with 3 internal nonwoven layers was analysed to
270 determine the deformation mechanisms and ascertained the benefits of the hybrid system
271 over the single material targets due to the interaction between layers. Distance between
272 the steel plates and the nonwoven was set to 30 mm. Meanwhile, nonwovens were regularly
273 spaced every 10 mm, resulting on a final shield thickness of 80 mm and a total areal weight

Table 3: Summary of tested configurations and numerical results.

Shield	Air gap (mm)	Areal density (g/m ²)	V_{50} (m/s)	Energy at V_{50} (J)
1 steel plate	—	5500	165	9.6
2 steel plates	80	11000	235	19.5
1 nonwoven	—	200	328	37.9
2 nonwovens	0.1	400	420	62.3
2 nonwovens	10	400	436	67.1
2 nonwovens	50	400	409	59.1
3 nonwovens	10	600	507	94.5
Hybrid	30/10/10/30	11600	745	195.9

of 11600 g/m².

Comparison of the different targets was carried out in terms of ballistic limit V_{50} , maximum energy absorption capacity and residual velocity curves obtained from an average of 8 simulations at different impact velocities. Relationship between the ballistic limit and the residual velocity was established by the Lambert-Jonas equation [22],

$$V_{res} = A(V_{ini}^n - V_{50}^n)^{1/n} \quad (9)$$

where V_{res} and V_{ini} are the residual and impact velocities as given by the simulations, respectively. The ballistic limit V_{50} , the exponent n and the constant A were parameters obtained by least squares fitting.

4. Results and discussion

The following section presents an analysis of the numerical simulations accomplished for the optimisation of the multilayer shield, and summary of numerical results is available in Table 3. Shield configuration, air gap spacing, areal weight, ballistic limit and energy absorbed at the ballistic limit have been included.

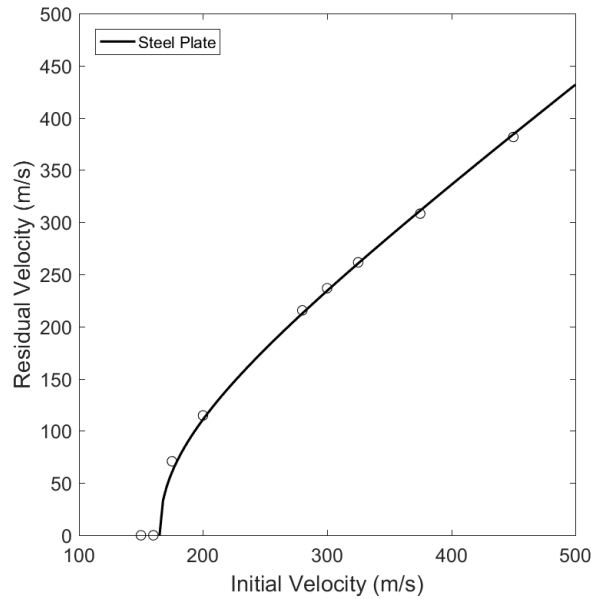


Figure 4: Numerical residual velocity curve of the steel plate with thickness 0.7 mm. The open circles stand for the numerical predictions and the line for eq.9.

287 *4.1. Impact performance of the steel plate*

288 Ballistic response of one single steel plate of 0.7 mm thickness was ascertained by simu-
 289 lation. The results in terms of the residual velocity, V_{res} , as a function of the initial velocity,
 290 V_{ini} , are plotted in Fig.4. Ballistic limit was predicted to be 165 m/s, with an energy absorp-
 291 tion capacity of 9.6 J for the given projectile. The loss of impact energy was mainly caused
 292 by the momentum transfer as a result of the high areal density of the steel plate. **Plastic**
 293 **deformation was localised at the impact point and different failure modes were registered for**
 294 **each velocity regime, as previously reported for thin ductile plates stricken by hemispherical**
 295 **projectiles [8]. Low velocity impact resulted in petalling due to the propagation of circum-**
 296 **ferential cracks preceding the formation of radial cracks, see Fig.5(a). As the impact velocity**
 297 **was further increased, the circumferential cracks produced a clean plug separation from the**
 298 **rest of the plate, see Fig.5(b).**

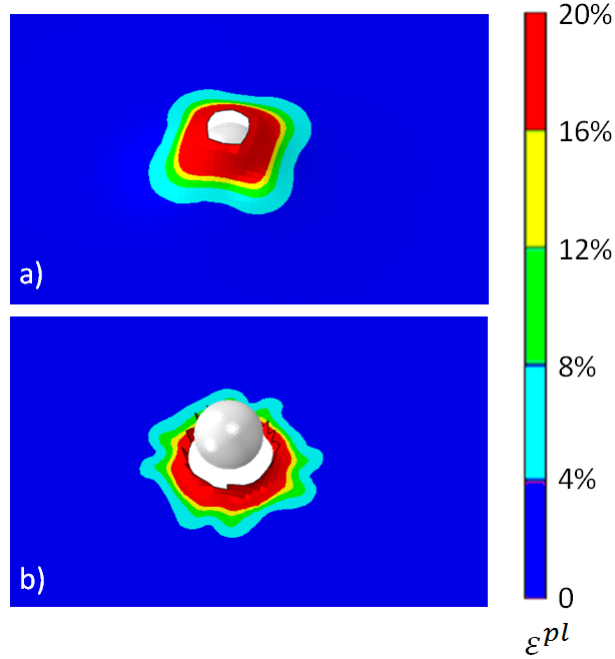


Figure 5: Contour plots of the equivalent plastic strain showing the failure modes of the steel plate for different impact velocity regimes. (a) Petalling failure mode near by the ballistic limit, $v_{ini}= 160$ m/s at $t = 400 \mu\text{s}$ and (b) shear plugging failure mode for high velocity impact, $v_{ini}= 900$ m/s at $t = 20 \mu\text{s}$.

299 4.2. Impact performance of the nonwoven fabric

300 The multiscale constitutive model presented above was used to simulate the impact
 301 behaviour of the as-received nonwoven fabric at different impact velocities. The results of
 302 the simulations, in terms of the residual velocity, V_{res} , as a function of the initial velocity, V_{ini} ,
 303 are plotted in Fig.6 together with the experimental results presented in [28]. As previously
 304 reported [27, 31, 32], the stochastic definition of the fibre pull-out strength promoted a
 305 numerical scattering of the predicted residual velocities. The constitutive model was able to
 306 capture accurately the ballistic limit of the nonwoven shield and the dominant deformation
 307 and failure micromechanisms, however, the numerical simulations tended to underestimate
 308 the residual velocity of the projectile above the ballistic limit as failure due to thermal
 309 softening of the Dyneema fibres was not included in the model formulation. Maximum
 310 energy absorption capacity was characterised as 37.9 J for the given projectile corresponding
 311 to a ballistic limit of 328 m/s. Although the nonwoven possessed a higher ballistic limit than

312 their counterpart steel plate, it presented a relatively low energy absorption capacity above
313 the ballistic limit, characteristic of dry fabrics [9].

314 The multiscale model replicated the deformation and failure micromechanisms, predict-
315 ing accurately the wave propagation phenomena during the impact. The model was able
316 to compute the mechanical response of the fabric from the discrete response of the fibres
317 contained in the fibre network, providing detailed evolution of straightening, realignment
318 and sliding for each set of fibre orientations [31]. Energy was dissipated by the tensile de-
319 formation of the fabric around the impact point in an elliptical region whose boundaries
320 were controlled by the wave propagation with different velocities along TD and MD, see
321 Fig.7(c). Higher strains appeared at the stiffest direction of the material, as previously re-
322 ported experimentally during impact on anisotropic plates [39]. The transverse wave was
323 also properly captured, showing the large deformability and low bending stiffness of the
324 material, see Fig.7(a) and (b). The ratio of the major to the minor axis of the cross-section
325 in the simulation was 1.6, close to the experimental value of 2 previously reported [28]. Final
326 penetration of the fabric around the ballistic limit occurred by fibre disentanglement from
327 the fabric network around the impact point, see Fig.8. This failure mechanism, although
328 affected a low fraction of fibres, was able to absorb a significant amount of energy due to
329 the high length of the fibres (50 to 60 mm long).

330 *4.2.1. Influence of the spacing between layers*

331 A detailed study has been carried out to understand the influence of the spacing between
332 layers in the energy absorption capacity of the multilayer nonwoven shield. Numerical models
333 composed by two nonwoven plies positioned at distances ranging from 0.1 to 50 mm every
334 2 mm were implemented. Predicted residual velocities *vs* spacing between layers for an
335 initial impact velocity of 450 m/s is depicted in Fig.9. **Different residual velocities were**
336 **predicted depending on the interaction between layers.** Increasing the spacing between
337 layers, from 0.1 up to 10 mm progressively increased the energy absorption capacity of the
338 target, maintained up to 30 mm spacing. Scatter in energy absorption within this range
339 can be explained considering the variability of the predicted residual velocities observed in

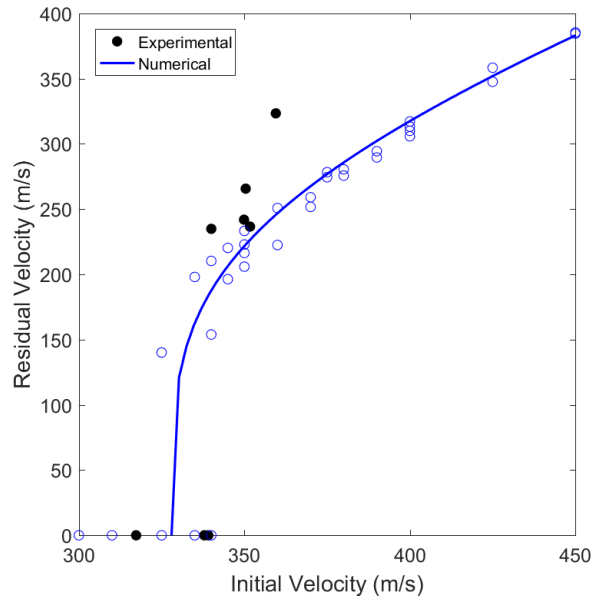


Figure 6: Experimental and numerical residual velocity curves of the nonwoven fabric. The solid circles stand for experimental results, the open circles for the numerical predictions and the line for eq.(9).

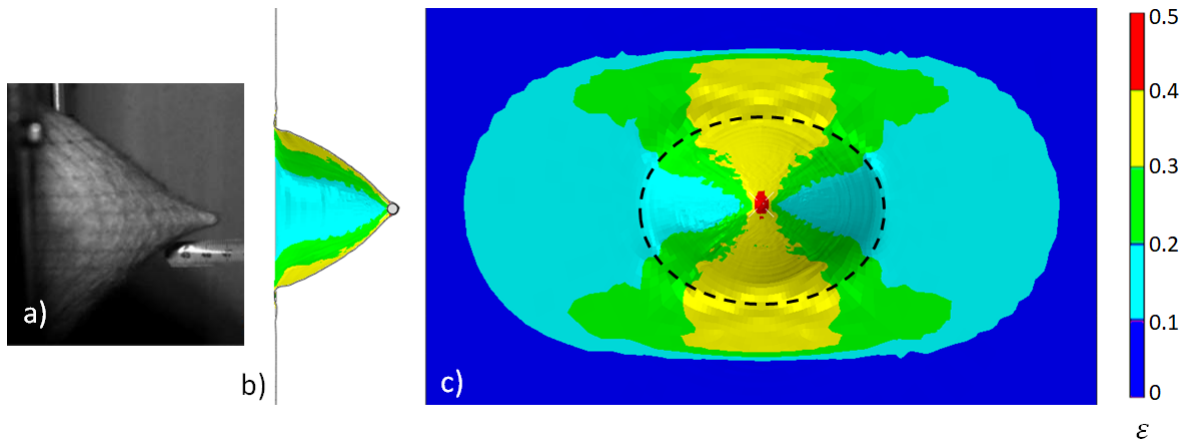


Figure 7: Global deformation of a $350 \times 350 \text{ mm}^2$ nonwoven target impacted by a small steel sphere of 5.5 mm diameter. Comparison between (a) experimental deflection and numerical (b) transverse and (c) longitudinal strain waves for the nonwoven fabric impacted at 300 m/s at $t = 500 \mu\text{s}$, below the ballistic limit. Contour plot of the maximum principal logarithmic strain. The broken line in the figure stand for the boundary of the transverse wave front.

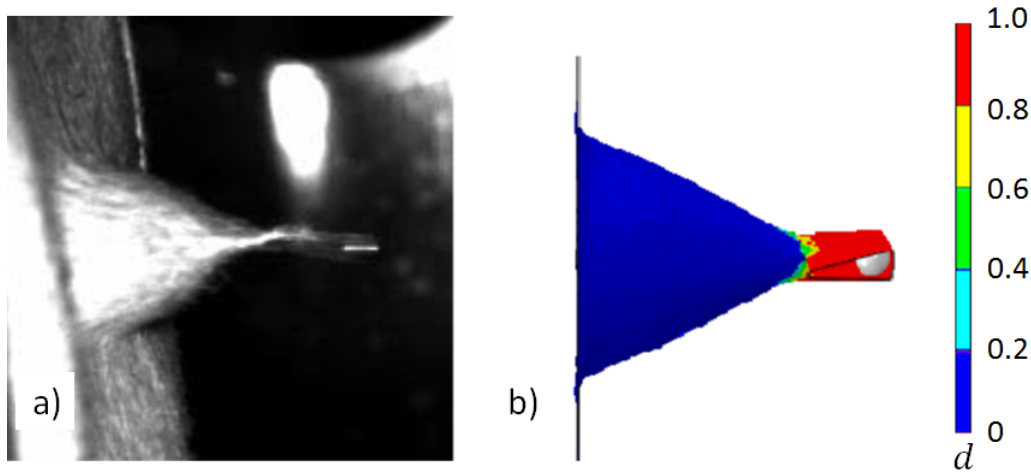


Figure 8: Lateral view of the nonwoven fabric during the impact at 360 m/s at 175 μ s above the ballistic limit, leading to the penetration of the fabric, (a) experimental photograph and (b) contour plot of the damage variable. The zones in red in the contour plots are representative of a fully disentangled fabric. [31].

340 previous publications due to the stochastic implementation of the fibre pull-out strength
 341 [31]. Further increment of the gap between layers resulted in a progressive loss of the
 342 energy absorption capacity up to 40 mm, where the residual velocity remained constant and
 343 independent of this particular design parameter as the physical interaction between plies
 344 was prevented. Ballistic curves for 0.1, 10 and 50 mm distance configurations are compared
 345 in Fig.10, showing similar trends for residual velocities ranging from 400 to 550 m/s. The
 346 response of a single layer has been included as reference. The ballistic limit increased when
 347 increasing the areal weight of the shield, however, the maximum ballistic limit was found for
 348 the configuration with 10 mm gap, which also presented superior energy absorption capacity
 349 for higher impact velocities. Intermediate energy dissipation was found for 0.1 mm spacing,
 350 meanwhile, the lower performance appeared for the 50 mm configuration.

351 Ballistic behaviours were classified in three different categories, depending on the in-
 352 teraction between layers during impact. Ballistic response of the no clearance target (0.1
 353 mm gap) initially behaved as a single layer shield with double density, see Fig.11(a). The
 354 interaction between layers became significant once fibre pull-out developed. At this point,
 355 higher stresses appeared on the unconstrained rear layer, which failed prematurely due to

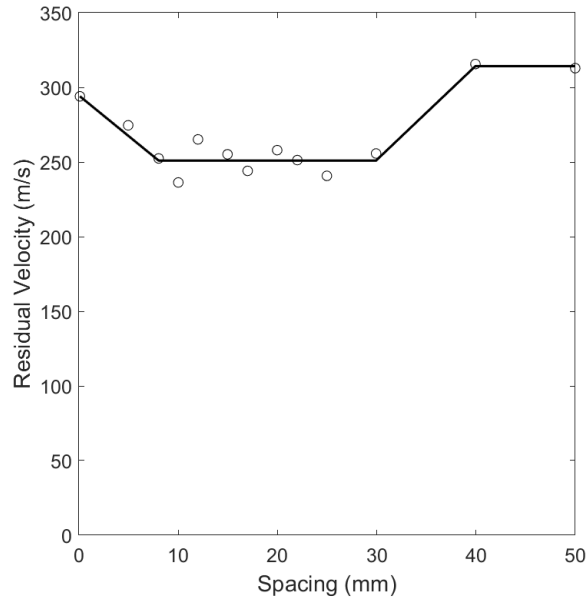


Figure 9: Residual velocity of the projectile *vs* spacing between layers for shields composed by 2 nonwoven layers impacted at 450 m/s. The circles stand for the numerical predictions and the line for the trend curve.

356 fibre disentanglement, see Fig.11(b). This produced a confinement of the fibres of the front
357 layer, increasing the fibre alignment and energy absorption capacity until final failure of
358 the shield, see Fig.11(c). Similar behaviour in hybrid shields was reported in [32]. As the
359 spacing between layers is progressively increased, a substantial change in the main failure
360 mechanism was observed. For intermediate distances (e. g. 10 mm spacing) in a first stage
361 of the impact, contact of the projectile with the front layer happened, and deformation
362 progressed as observed for the single layer case. As the deflection increased, both layers
363 came in contact and structurally worked together to arrest the projectile, see Fig.11(d).
364 Further deformation initiated the fibre pull-out of the first impacted layer, however, the
365 rear nonwoven, undamaged, contributed to delay the penetration of the first ply, increasing
366 the energy absorbed. After penetration of the front layer, fibre pull-out was induced on
367 the rear layer, see Fig.11(e). Finally the model predicted a total fibre disentanglement, see
368 Fig.11(f). This synergistic contribution was observed up to 30 mm spacing between layers.
369 For configurations with larger gaps, the layer interaction decreased, and beyond 40 mm, the

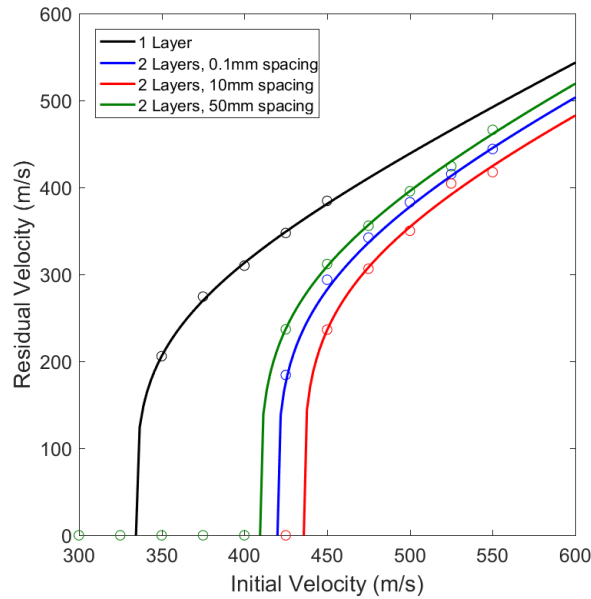


Figure 10: Residual velocity curves for 2 layers nonwoven shields with spacing 0.1, 10 and 50 mm and comparison with the single layer nonwoven. The circles stand for the numerical predictions and the lines for eq.(9).

370 failure of the layers happened individually, as the front layer failed before contacting the
 371 rear one, see Fig.11(h). Therefore, the second layer did not contribute to delay the failure
 372 of the first layer and led to a lower impact performance.

373 The numerical simulations also provided quantitative measurements of the energy ab-
 374 sorbed by each layer, justifying the differences in ballistic performance. Fig.12 shows the
 375 percentages of strain and kinetic energies transferred to the front and rear layers of the shield
 376 during an impact of initial velocity 450 m/s for 0.1, 10 and 50 mm spacing. Evolution of
 377 the kinetic energy of the projectile is also depicted for comparison purposes, see Fig.12(e).
 378 Frictional dissipation was determined as a 3% of the initial kinetic energy and has not been
 379 included in the graphs for the sake of clarity. Artificial energies due to hourglass and element
 380 distortion control were maintained below 10% of the total energy of the system. Deformation
 381 and failure mechanisms can be analysed through these graphs. On the initial stage of the
 382 impact, strain and kinetic energies were homogeneously transmitted to the layers as a result

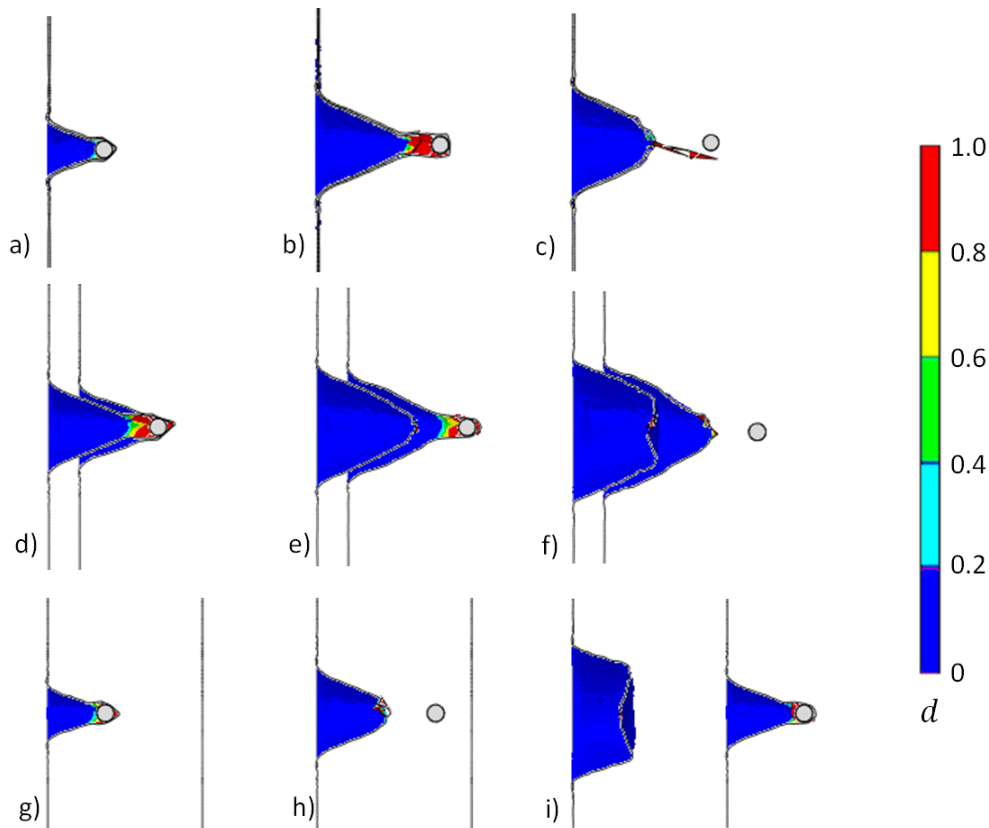


Figure 11: Failure sequence and contour plot of the damage variable for the two-layer shields impacted at 450 m/s. (a), (b) and (c), 0.1 mm spacing at $t=50 \mu s$, $t=120 \mu s$ and $t=150 \mu s$, respectively. (d), (e) and (f), 10 mm spacing at $t=100 \mu s$, $t=150 \mu s$ and $t=200 \mu s$, respectively. (g), (h) and (i), 50 mm spacing at $t=50 \mu s$, $t=100 \mu s$ and $t=200 \mu s$, respectively. The zones in red in the contour plots are representative of a fully disentangled fabric.

383 of the progressive fibre straightening and alignment produced by the longitudinal and trans-
 384 verse waves. At a certain point of the simulation, pull-out stress threshold of the fibres was
 385 overtaken and the projectile produced significant fibre disentanglement. Penetration was
 386 virtually represented by element deletion, which generated a release elastic wave, decreasing
 387 the stored strain energy, see Figs.12(a) and (b), which was suddenly transformed into an
 388 excess of kinetic energy dissipated by viscous damping to avoid numerical instabilities, see
 389 Figs.12(c) and (d).

390 The configuration with 10 mm gap presented higher energy absorption capacity in terms
 391 of both strain and kinetic energies, as a result of the beneficial interaction between layers.

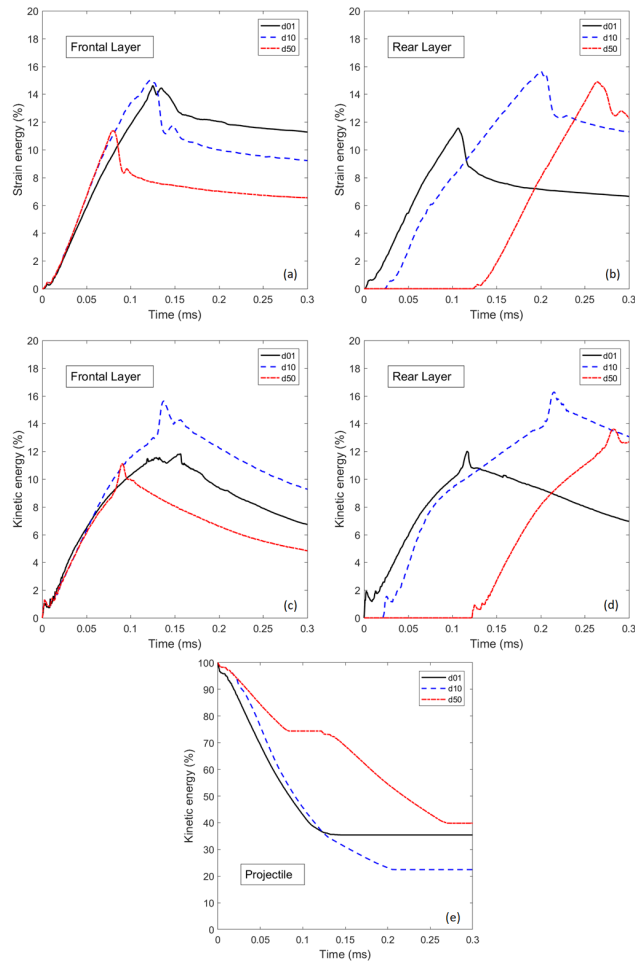


Figure 12: Numerical predictions of the evolution of the energy absorption of the two-layer shields during an impact at 450 m/s with spacing 0.1, 10 and 50 mm. (a), (b) strain energy and (c) and (d) kinetic energy of the front and rear layers, respectively. (e) Evolution of the kinetic energy of the projectile.

392 Initially the energy absorption rate was similar for all layers in all configurations, as shown
 393 by the slopes of the energy evolution curves. As a result of this, the longer the contact
 394 time between projectile and shield, the higher the energy absorbed. This fact explains why
 395 delaying the final failure of a layer becomes so critical to improve the ballistic performance
 396 of the shield. The zero-clearance configuration, 0.1 mm gap, tended to decrease the rate of
 397 energy absorption and the momentum transferred as the motion of layers was constrained.
 398 At the opposite end, the configuration with the largest gap, 50 mm, worked as two individual
 399 systems and presented a premature penetration. Finally, the configuration based on a 10 mm

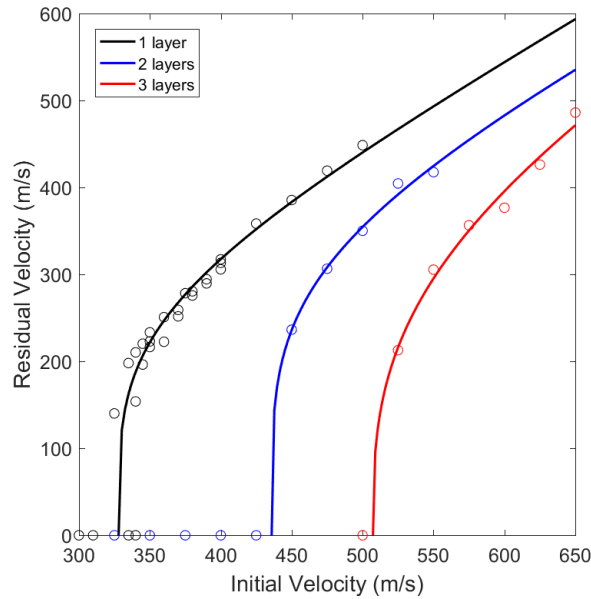


Figure 13: Residual velocity curves for nonwoven targets with 10 mm spacing between layers composed by 1, 2 and 3 layers. The circles stand for the numerical predictions and the lines for eq.(9).

400 gap distance presented the optimal results due to the synergistic interaction of the layers.
 401 Clearly, the rear layer contributed to delay the penetration of the front layer, increasing
 402 both, strain and kinetic energies transferred to the target during the impact. Overall, for
 403 the given impact energy, this configuration absorbed an additional 12% of energy compared
 404 to their counterparts.

405 Considering the space constraint given by the width of the vehicle door, 10 mm air
 406 gap was selected to analyse the response of the three-layer nonwoven shield configuration
 407 for future implementation in the automotive component. This distance offered the higher
 408 energy absorption capacity (characterised in the region 10 to 30 mm) with the minimum
 409 spacing. Fig.13 shows the residual velocity curve together with the single- and two-layered
 410 target. Increasing the areal weight of the protection increased the ballistic limit and energy
 411 absorption capacity of the shield, up to a maximum of 94.5 J. Failure sequence is reported
 412 in Fig.14. The same failure mechanisms as in the previous two-layered configuration were
 413 found. Large fibre pull-out was observed, with all layers contributing to delay the final dis-

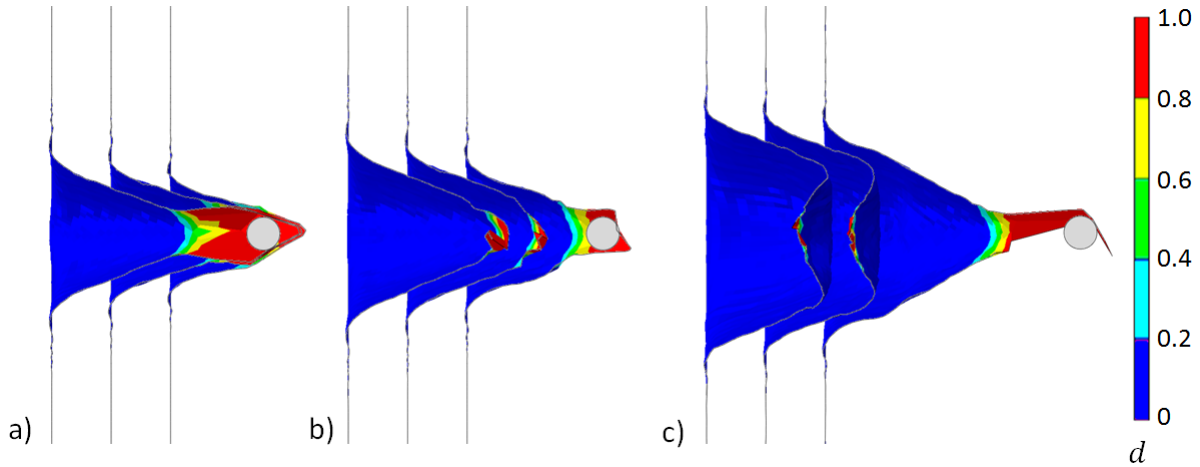


Figure 14: Failure sequence and contour plot of the damage variable for the three-layer shields with 10 mm spacing impacted at 550 m/s. (a) $t=80 \mu\text{s}$, (b) $t=100 \mu\text{s}$ and (c) $t=160 \mu\text{s}$. The zones in red in the contour plots are representative of a fully disentangled fabric.

414 entanglement, see Fig.14(a). As deformation progressed, the frontal and intermediate layers
 415 failed simultaneously, see Fig.14(b), with final disentanglement of the rear layer afterwards,
 416 as depicted in Fig.14(c).

417 4.3. Impact performance of multi-layered shields

418 Finally, the steel plates and nonwoven fabrics were combined in a multi-layered protective
 419 shield for automotive applications, and the ballistic performance of the system was evaluated
 420 by means of numerical simulations. The shield was composed by two external steel plates
 421 and 3 internal nonwovens with a total thickness of 80 mm as specified in Section 3.3. Fig.15
 422 compares the residual velocity curves of the multi-layered target with the performance of its
 423 individual components; the steel plates and the nonwoven layers. Although the areal weight
 424 of the three nonwovens (600 g/m^2) was about 20 times smaller than the one of the 2 steel
 425 plates (11000 g/m^2), a remarkable increment of the ballistic limit of 250 m/s approximately
 426 was obtained. Furthermore, the multi-layered system outperformed the previous configura-
 427 tions in terms of ballistic limit and of the energy dissipated, which almost doubled the sum
 428 of the energies dissipated individually by the steel plates (19.5 J) and nonwoven fabrics (94.5
 429 J), resulting in an outstanding 195.9J of energy absorption capacity for the given projectile.

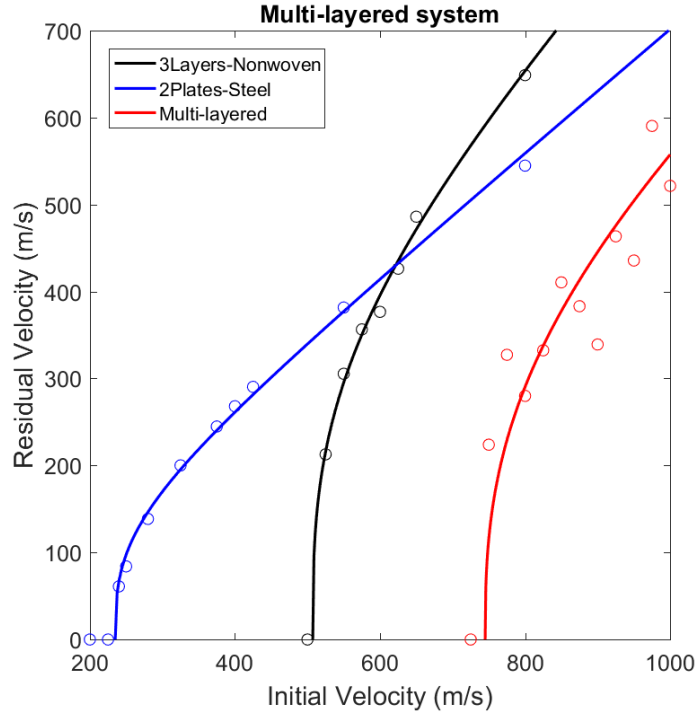


Figure 15: Residual velocity curves for 2 plates of steel (11000 g/m^2 areal weight), 3 layers of nonwoven at 10 mm spacing (600 g/m^2 areal weight) and the combined multi-layered shield composed by the 2 plates plus the 3 intermediate nonwoven layers (11600 g/m^2 areal weight). The circles stand for the numerical predictions and the lines for eq.(9).

430 It is also worth mentioning that the multi-layered shield increased the energy absorption by
 431 a factor over 8 with respect to the steel configuration with a negligible increment of weight
 432 of 5.5%.

433 The large deformation of the nonwoven layers and their synergistic interaction between
 434 nonwoven fabrics and metal plates led to this outstanding increment of energy absorption.
 435 During the first stage of the impact, the projectile pierced the front steel plate and im-
 436 pacted the nonwoven layers, which deflected together dissipating a significant fraction of
 437 the projectile's energy. As it was observed previously for the three- layered shields, the rear
 438 nonwoven layers contributed to delay the fibre disentanglement of the front ones, increasing
 439 the energy absorbed by all the plies. Further deflection of the layers resulted in the contact
 440 of the projectile with the rear steel plate, which not only delayed the failure of the internal

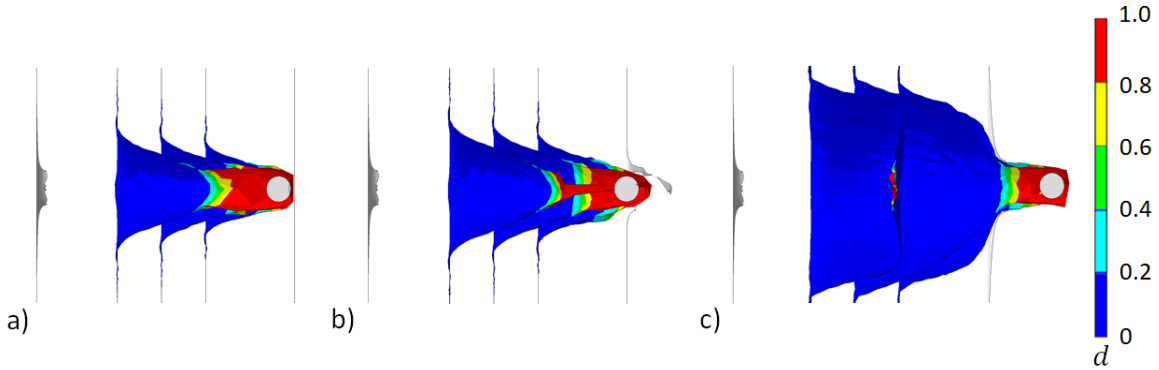


Figure 16: Failure sequence and contour plot of the damage of the multi-layered shield based on two external steel plates and three internal nonwoven layers impacted at 725 m/s. (a) $t=90 \mu\text{s}$ (b) $t=135 \mu\text{s}$ and (c) $t=225 \mu\text{s}$. The zones in red in the contour plots are representative of a fully disentangled fabric. In this simulation, the projectile was fully arrested after $\approx 300 \mu\text{s}$.

441 nonwovens, see Fig.16(a), but also transferred momentum and energy to the plate. The
 442 interaction between these nonwovens and the rear plate induced higher plastic deformation
 443 on the steel when compared to the front plate. For impact velocities just below the bal-
 444 listic limit, penetration of the steel plate occurred and the projectile pulled the nonwoven
 445 through the generated breach, resulting in a confinement of the material and a massive fi-
 446 bre alignment and rotation towards the loading direction localised at the impact point, see
 447 Fig.16(b). This confinement of the nonwoven fabric led to an extra absorption of energy and
 448 a progressive decrement of the projectile velocity, which finally got arrested by the ballistic
 449 protection, see Fig.16(c).

450 Although nonwovens absorbed energy by both material deformation and momentum
 451 transfer, the metal plates mainly reduced the kinetic energy of the projectile due to the
 452 latter mechanism. Fig.17 shows the comparison of the evolution of kinetic energy of the
 453 projectile when impacting the baseline metal plates and the hybrid configurations with an
 454 impact velocity of 725 m/s. Contact between projectile and layers has been identified by
 455 dashed lines. Impact with the steel plates alone produced a sudden drop of the energy of the
 456 projectile. Despite this mechanism absorbed a significant amount of energy, it was definitely
 457 insufficient to arrest the projectile. On the other hand, the hybrid shield presented a complex

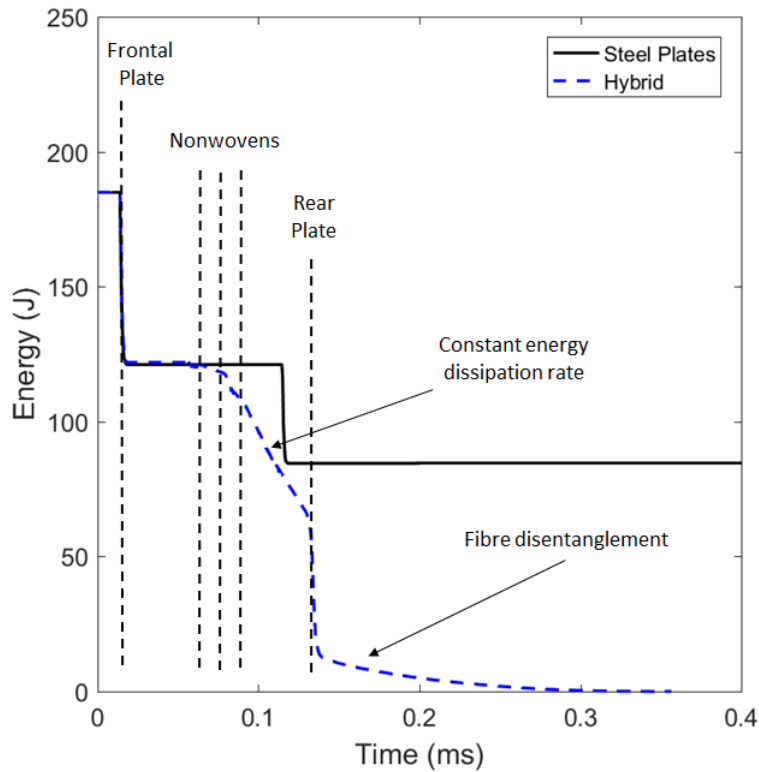


Figure 17: Evolution of the kinetic energy of the projectile when impacting the baseline metal configuration and the hybrid shield with an impact velocity of 725 m/s. The dashed lines indicate the contact points between projectile and layers for the hybrid configuration.

458 response, that can be divided in four different stages. Initially, the projectile **struck** the
 459 metal plate as in the previous configuration. Afterwards, progressive energy dissipation was
 460 controlled by the nonwovens. Energy absorption increased as nonwovens engaged during
 461 the impact, resulting in a constant energy dissipation rate over an extended period of time.
 462 Further deformation produced the contact with the rear steel plate, inducing a sudden drop
 463 of kinetic energy during penetration. The final energy absorption mechanism was fibre
 464 disentanglement of the confined material inside the metal plate perforation. Although the
 465 fraction of fibres involved in this mechanism was relatively small, the extra time needed
 466 for the fibre extraction resulted in a significant energy dissipation, that finally arrested the
 467 projectile.

468 5. Conclusions

469 The impact response of a hybrid shield composed by external metal plates and internal
470 nonwoven fabrics has been numerically studied. Ballistic performance in terms of residual
471 velocity curves was analysed for impacts with steel spheres of 5.5 mm in diameter for a
472 wide range of initial velocities. Steel plates were modelled by a standard elastic-plastic
473 constitutive law at an homogenised macroscopic level, while the response of the nonwoven
474 fabric was defined by a multiscale constitutive model, able to take into account the complex
475 deformation and fracture mechanisms during impact. Ballistic response of each material was
476 analysed individually. The thin steel plates presented a limited energy absorption capacity
477 due to their low thickness. The main energy absorption mechanism was momentum transfer
478 and plastic deformation, localised at the impact point. The nonwoven fabric presented a
479 higher ballistic limit than the metal plate, although energy absorption capacity was rapidly
480 reduced beyond that point. The identified absorption mechanisms were the momentum
481 transferred to the fabric, fibre realignment and straightening due to the longitudinal wave
482 propagation and fibre pull-out. These findings were in agreement with experimental data
483 previously reported in the literature for both, thin ductile metal plates and nonwovens [8, 31].

484 Special attention was paid to the interaction between layers for different air gaps in the
485 final energy absorption capacity of the shield. The influence of spacing was analysed for two
486 and three nonwoven layered targets. Intermediate gap distances, between 10 and 30 mm,
487 were beneficial in terms of ballistic limit and final energy absorption. This gap induced a
488 synergistic interaction between layers where the rear ply contributed to delay the final disen-
489 tanglement of the front layers and therefore produced an increment of the energy transferred
490 to the shield. Quantitatively, the 10 mm gap separation offered an additional 12% of energy
491 dissipation when compared to large gap (50 mm) or no clearance (0.1 mm) configurations.
492 Analysis of the energy absorbed by each layer showed how critical the contact time between
493 projectile and target was to improve the ballistic performance of the shield. Similar failure
494 sequences were observed for the hybrid shield composed by external steel plates and internal
495 nonwoven fabrics. The hybrid system outperformed the previous configurations, resulting in

496 an outstanding energy absorption capacity, about twice the sum of the energies dissipated
497 by the steel plates and the nonwovens individually. Furthermore, the hybrid shield increased
498 the energy absorption capacity of the baseline steel plates by a factor over 8, with a negli-
499 gible increment of areal weight of a 5.5%. Thus, this kind of hybrid shields are an efficient
500 lightweight solution to arrest small fragments in the automotive sector. Once again, all the
501 layers of the system contributed to delay the catastrophic failure of the shield increasing the
502 energy absorbed. For velocities close to the ballistic limit, the projectile was able to pene-
503 trate the rear steel plate, however, the large deformability of the nonwoven and the extra
504 energy dissipation induced due to the material confinement finally arrested the projectile.

505 **6. Acknowledgement**

506 This investigation was supported by the Universidad Politécnica de Madrid through
507 "Programa Propio 2018" [grant number VJIDOCUPM18ARR]. In addition, FMH acknowl-
508 edges the support of the University of Edinburgh through the start-up funding for recently
509 appointed Lecturers.

- 510 [1] Abtew, M. A., Boussu, F., Bruniaux, P., Loghin, C., Cristian, I., 2019. Ballistic impact mechanisms-a
511 review on textiles and fibre-reinforced composites impact responses. *Composite Structures*, 110966.
- 512 [2] Alderliesten, R., 2015. Designing for damage tolerance in aerospace: A hybrid material technology.
513 *Materials & Design* 66, 421–428.
- 514 [3] ArcelorMittal, 2018. Bake hardening steels.
515 URL <http://corporate.arcelormittal.com/>
- 516 [4] B. A. Cheeseman, T. A. B., 2003. Ballistic impact into fabric and compliant composite laminates.
517 *Composite Structures* 61 (1-2), 161–173.
- 518 [5] Bansal, S., Mobasher, B., Rajan, S. D., Vintilescu, I., 2009. Development of Fabric Constitutive Be-
519 havior for Use in Modeling Engine Fan Blade-Out Events. *Journal of Aerospace Engineering* 22 (3),
520 249–259.
- 521 [6] Chen, N., Silberstein, M. N., 2019. A micromechanics-based damage model for non-woven fiber net-
522 works. *International Journal of Solids and Structures* 160, 18–31.
- 523 [7] Chocron, S., Pintor, A., Cendón, D., Gálvez, F., Sánchez-Gálvez, V., 2002. Simulation of ballistic
524 impact in a polyethylene non-woven felt. In: *20Th International Symposium on Ballistics*. Orlando, pp.
525 23–27.

- 526 [8] Corbett, G. G., Reid, I. S. R., Johnson, W., 1996. Impact Loading of Plates and Shells by Free-flying
527 Projectiles: A Review. *International Journal of Impact Engineering* 18 (2), 141–230.
- 528 [9] Cunniff, P. M., 1992. An analysis of the system effects in woven fabrics under ballistic impact. *Textile*
529 *Research Journal* 62 (9), 495–509.
- 530 [10] Das, A., Tarafder, S., Sivaprasad, S., Chakrabarti, D., 01 2015. Effect of strain rate on bake hardening
531 response of BH220 steel. *EPJ Web of Conferences* 94, 01037.
- 532 [11] Dassault Systemes. *Abaqus 6.10 User's Manual*, 2010.
- 533 [12] Deng, Y., Zhang, W., Cao, Z., 2012. Experimental investigation on the ballistic resistance of monolithic
534 and multi-layered plates against hemispherical-nosed projectiles impact. *Materials & Design* 41, 266–
535 281.
- 536 [13] Destefanis, R., Schäfer, F., Lambert, M., Faraud, M., 2006. Selecting enhanced space debris shields for
537 manned spacecraft. *International Journal of Impact Engineering* 33 (1-12), 219–230.
- 538 [14] Garijo, D., Martínez-Hergueta, F., Lopes, C. S., Llorca, J., González, C., Puente, J. L., Loya, J. A.,
539 Toral-Vázquez, J., Votsios, V., Martino, E., 2018. Multiscale FE Modelling and Design of Composite
540 Laminates Under Impact. In: *Comprehensive Composite Materials II*. Vol. 8. pp. 219–238.
- 541 [15] Guo, Y. B., Chiang, H. J., Deng, J. J., Shim, V. P., 2019. Projectile impact on fabric-metal assemblies
542 Influence of fabric-metal sequence. *International Journal of Impact Engineering* 127 (December 2018),
543 1–16.
- 544 [16] He, Z., Xuan, H., Bai, C., Hu, Y., Cong, P., Bai, H., 2017. Containment tests and analysis of soft wall
545 casing fabricated by wrapping Kevlar fabric around thin metal ring. *Aerospace Science and Technology*
546 61, 35–44.
- 547 [17] Hooputra, H., Gese, H., Dell, H., Werner, H., 2004. A comprehensive failure model for crashworthiness
548 simulation of aluminium extrusions. *International Journal of Crashworthiness* 9 (5), 449–464.
- 549 [18] Ipson, T. W., Wittrock, E. P., 1966. Response of non-woven synthetic fiber textiles to ballistic impact.
550 Tech. rep., No. TR-67-8-CM. Denver Research Institute.
- 551 [19] Kiliç, N., Ekici, B., 2013. Ballistic resistance of high hardness armor steels against 7 . 62 mm armor
552 piercing ammunition. *Materials and Design* 44, 35–48.
- 553 [20] Kiran, R., Khandelwal, K., 2014. A triaxiality and lode parameter dependent ductile fracture criterion.
554 *Engineering Fracture Mechanics* 128, 121–138.
- 555 [21] Krishnan, K., Sockalingam, S., Bansal, S., Rajan, S. D., 2010. Numerical simulation of ceramic com-
556 posite armor subjected to ballistic impact. *Composites Part B: Engineering* 41 (8), 583–593.
- 557 [22] Lambert, J., Jonas, G., 1976. Towards standardization in terminal ballistics testing: velocity represen-
558 tation. Tech. rep., Army Ballistic Research Lab. Aberdeen.
- 559 [23] Lim, C., Shim, V., Ng, Y., 2003. Finite-element modeling of the ballistic impact of fabric armor.

- 560 International Journal of Impact Engineering 28 (1), 13–31.
- 561 [24] Liu, J., Long, Y., Ji, C., Liu, Q., Zhong, M., Zhou, Y., 2018. Influence of layer number and air gap
562 on the ballistic performance of multi-layered targets subjected to high velocity impact by copper EFP.
563 International Journal of Impact Engineering 112, 52–65.
- 564 [25] Liu, P., Zhu, D., Yao, Y., Wang, J., Bui, T. Q., 2016. Numerical simulation of ballistic impact behavior
565 of bio-inspired scale-like protection system. Materials & Design 99, 201–210.
- 566 [26] Marino, M., Wriggers, P., 2019. Micro–macro constitutive modeling and finite element analytical-based
567 formulations for fibrous materials: A multiscale structural approach for crimped fibers. Computer
568 Methods in Applied Mechanics and Engineering 344, 938–969.
- 569 [27] Martínez-Hergueta, F., 2016. Multiscale analysis of the mechanical behavior of needle-punched nonwo-
570 ven fabrics. Ph.D. thesis, Polytechnic University of Madrid.
- 571 [28] Martínez-Hergueta, F., Ridruejo, A., Gálvez, F., González, C., LLorca, J., 2016. Influence of fiber
572 orientation on the ballistic performance of needlepunched nonwoven fabrics. Mechanics of Materials 94,
573 106–116.
- 574 [29] Martínez-Hergueta, F., Ridruejo, A., González, C., LLorca, J., 2015. Deformation and energy dissipa-
575 tion mechanisms of needle-punched nonwoven fabrics: A multiscale experimental analysis. International
576 Journal of Solids and Structures 65, 120–131.
- 577 [30] Martínez-Hergueta, F., Ridruejo, A., González, C., LLorca, J., 2016. Multiscale micromechanical model
578 for needlepunched nonwoven fabrics. International Journal of Solids and Structures 96, 81–91.
- 579 [31] Martínez-Hergueta, F., Ridruejo, A., González, C., Llorca, J., 2017. Numerical simulation of the ballistic
580 response of needle-punched nonwoven fabrics. International Journal of Solids and Structures 106-107,
581 56–67.
- 582 [32] Martínez-Hergueta, F., Ridruejo, A., González, C., LLorca, J., 2018. Ballistic performance of hybrid
583 nonwoven/woven polyethylene fabric shields. International Journal of Impact Engineering 111, 55–65.
- 584 [33] Naik, D., Sankaran, S., Mobasher, B., Rajan, S., Pereira, J., 2009. Development of reliable modeling
585 methodologies for fan blade out containment analysis Part I: Experimental studies. International
586 Journal of Impact Engineering 36 (1), 1–11.
- 587 [34] Pandya, K. S., Pothnis, J. R., Ravikumar, G., Naik, N., 2013. Ballistic impact behavior of hybrid
588 composites. Materials & Design 44, 128–135.
- 589 [35] Qiao, P., Yang, M., Bobaru, F., 2008. Impact Mechanics and High-Energy Absorbing Materials :Review.
590 Journal of Aerospace Engineering 21 (October), 235–248.
- 591 [36] Ridruejo, A., González, C., LLorca, J., 2012. A constitutive model for the in-plane mechanical behavior
592 of nonwoven fabrics. International Journal of Solids and Structures 49 (17), 2215–2229.
- 593 [37] Russell, S. J., 2007. Handbook of nonwovens. The Textile Institute. Woodhead Publishing.

- 594 [38] Sadighi, M., Alderliesten, R. C., Benedictus, R., 2012. Impact resistance of fiber-metal laminates: A
595 review. *International Journal of Impact Engineering* 49, 77–90.
- 596 [39] Seidt, J. D., Pereira, J. M., Gilat, A., Revilock, D. M., Nandwana, K., 2013. Ballistic impact of
597 anisotropic 2024 aluminum sheet and plate. *International Journal of Impact Engineering* 62, 27–34.
- 598 [40] Shen, C., Dumbleton, J., 1974. The friction and wear behavior of irradiated very high molecular weight
599 polyethylene. *Wear* 30 (3), 349–364.
- 600 [41] Shim, V., Tan, V., Tay, T., 1995. Modelling deformation and damage characteristics of woven fabric
601 under small projectile impact. *International Journal of Impact Engineering* 16 (4), 585–605.
- 602 [42] Shockey, D. A., Erlich, D. C., Simons, J. W., 1999. Lightweight Fragment Barriers for Commercial
603 Aircraft. 18Th International Symposium on Ballistics, 15–19.
- 604 [43] Sinmazçelik, T., Avcu, E., Özgür, M., Çoban, O., 2011. A review: Fibre metal laminates, background,
605 bonding types and applied test methods. *Materials and Design* 32, 3671–3685.
- 606 [44] Stahlecker, Z., Mobasher, B., Rajan, S., Pereira, J., 2009. Development of reliable modeling method-
607 ologies for engine fan blade out containment analysis. Part II: Finite element analysis. *International*
608 *Journal of Impact Engineering* 36 (3), 447–459.
- 609 [45] Tabiei, A., Nilakantan, G., 2008. Ballistic impact of dry woven fabric composites: A review. *Applied*
610 *Mechanics Reviews* 61 (1), 010801.
- 611 [46] Thoma, K., Schäfer, F., Hiermaier, S., Schneider, E., 2004. An approach to achieve progress in space-
612 craft shielding. *Advances in Space Research* 34 (5), 1063–1075.
- 613 [47] Thomas, H. L., Bhatnagar, A., Wagner, L. L., 2003. Needle-Punched Non-Woven for High Fragment
614 Protection. In: 14th International Conference of Composite Materials. San Diego, California.
- 615 [48] Vila-Ortega, J., 2018. Simulation of the ballistic impact on multilayer polyethylene nonwoven system.
616 Master's thesis, Technical University of Madrid.
- 617 [49] Wang, Q., Chen, Z., Chen, Z., 2013. Design and characteristics of hybrid composite armor subjected
618 to projectile impact. *Materials & Design* 46, 634–639.
- 619 [50] Yaghoubi, A. S., Liaw, B., 2012. Thickness influence on ballistic impact behaviors of GLARE 5 fiber-
620 metal laminated beams : Experimental and numerical studies. *Composite Structures* 94 (8), 2585–2598.